Chapter 10
The Dynamics of Unstable Waves

Kody J.H. Law and Q. Enam Hoq

10.1 Introduction

Discretized equations in which the evolution variable is continuous while the spatial variables are confined to points on the lattice, have had a significant presence and impact across multiple disciplines [1–6] (cf. Chap. 8 for a review on experiments related to the DLNS equation). This should not be surprising considering that many natural processes and phenomena exhibit discrete structure [7–11]. As particular examples, we see that in physics the discrete nonlinear Schrödinger equation was used to model periodic optical structures [12], while in biology the Davydov equations model energy transfer in proteins [13]. These diverse phenomena are testament to the ubiquitousness of discrete regimes across diverse settings, and hence validate the need to study them. The study of discretized equations can be traced at least back to the work of Frenkel and Kontorova on crystal dislocations [14] and the Fermi–Pasta–Ulam problem [15]. The literature has since grown significantly to include novel and engaging ideas (e.g. [16–25]), and one of the points of interest is the dynamical behavior of solutions [26–28].

In this section, we investigate the dynamics of unstable wave solutions to the cubic discrete nonlinear Schrödinger (DNLS) in one, two, and three spatial dimensions which were described in the previous chapters. While these earlier chapters focused on the analysis of the existence and linear stability/instability of the relevant solutions, the present section sheds light into typical dynamical evolution examples to illustrate the outcome of the previously identified instabilities.

The equation of interest is

$$i\dot{u}_{\mathbf{n}} = -\epsilon\Delta_d u_{\mathbf{n}} + g|u_{\mathbf{n}}|^2 u_{\mathbf{n}} \tag{10.1}$$

where $u_{\mathbf{n}}$ is the complex lattice field with **n** being the vectorial lattice index, Δ_d is the standard d-dimensional discrete Laplacian extrapolated from a three-point stencil, ϵ is the inter-site (IS) coupling, and $g = -1$ in Sect. 10.2 while $g = 1$ in Sect. 10.3.2.

K.J.H. Law (✉)
University of Massachusetts, Amherst, MA, 01003, USA
e-mail: law@math.umass.edu

P.G. Kevrekidis, *The Discrete Nonlinear Schrödinger Equation*, STMP 232, 205–220, DOI 10.1007/978-3-540-89199-4_10,

The overdot represents the derivative with respect to the evolution variable (which, for example, could be z in the case of optical arrays, or t in BEC models). Also, we write $\mathbf{u} = (u_{\mathbf{n}_1}, \ldots, u_{\mathbf{n}_{N^d}})$, to denote the complex lattice field of N sites in each of d dimensions.

As before, we are interested in stationary solutions of the form

$$u_{\mathbf{n}} = \exp(i\Lambda t)v_{\mathbf{n}} \tag{10.2}$$

for all $\mathbf{n}$. It can easily be seen that Eq. (10.1) admits such solutions in the anticontinuum (AC) limit ($\epsilon = 0$) with the additional structure $v_{\mathbf{n}} = e^{i\theta_{\mathbf{n}}}$ for $\theta_{\mathbf{n}} \in [0, 2\pi)$. This leads to the persistence as well as stability criteria detailed in the previous chapters (see also [29, 30] for further details). We look at solutions (from the previous chapters) for coupling values for which they have been predicted to be unstable. There exist parameter values such that an unstable solution of each configuration family eventually settles into a single site structure, and also that the time it takes for the original structure to break up is dependent on the magnitude of the real part of the linearization, the magnitude of the coupling between sites, and the initial perturbation.

The organization will be as follows. Section 10.2 will be devoted to 1(+1)-dimensional (10.2.1), 2(+1)-dimensional (10.2.2), and 3(+1)-dimensional (10.2.3) solutions of the standard focusing DNLS (Eq.(10.1) with $g = -1$). In Sect. 10.3, we discuss the more exotic settings of a grid with hexagonal geometry (10.3.1) and then solutions in the case of a defocusing nonlinearity ($g = +1$) in 1(+1) and 2(+1) dimensions (10.3.2). All the dynamical evolutions confirm stability predictions given theoretically and numerically in the preceding chapters, though some of the dynamical behavior is interesting and not a priori predictable.

10.2 Standard Scenario

We begin by discussing the space–time evolution of unstable solutions of the standard focusing DNLS (Eq. (10.1) with $g = -1$).

10.2.1 1(+1)*-Dimensional Solutions*

In this first section we examine the evolution of $\{|u_{\mathbf{n}}|^2\}$ (it is understood that the set is taken over all indices $\mathbf{n}$ in the d-dimensional lattice, where here $d = 1$ and the boldface is unnecessary, but we will use this notation throughout for consistency) for four one-dimensional configurations (see Fig. 10.1). Each is placed in the bulk of a lattice with 201 sites. Denoting a positive excited node by "+" and a negative one by "−", the configurations we consider are that of two in-phase (IP) adjacent nodes (i) $++$, and the following with three adjacent nodes (ii) $+++$, (iii) $++-$, and (iv) $+-+$. These can be found in Chap. 2. To expedite the onset of instability, in each

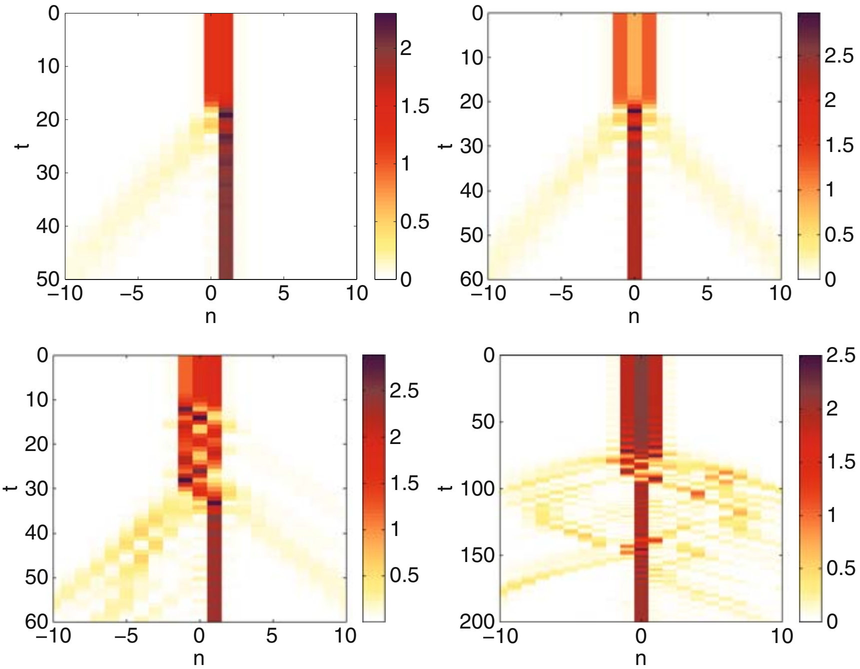

Fig. 10.1 These panels exhibit the space–time evolution of the density field $\{|u_{\mathbf{n}}(t)|^2\}$ of four modes to the one-dimensional DNLS equation. The *top left panel* shows the (i) $++$ configuration, the *top right* is (ii) $+++$, the *bottom left* is (iii) $++-$, and the bottom right is (iv) $+-+$

case the coupling parameter is $\epsilon = 0.3$, which is beyond the instability threshold of each configuration. We present the intensity of the field $\{|u_{\mathbf{n}}(t)|^2\}$, where $\mathbf{u} = \mathbf{u}_s + \mathbf{u}_r$, $\mathbf{u}_s$ being the lattice field with the respective stationary solution and $\mathbf{u}_r$ is a uniformly distributed random noise field in the interval $(0, a)$. For the discrete solitons (i)–(iv) above, The amplitude of the perturbation is taken to be (i) 10^{-8}, (ii) 10^{-7}, (iii) 10^{-5}, and (iv) 10^{-3}.

In all panels we clearly see a single surviving site that persists for long times. We see that the two IP modes dissolve from their original forms via a short turbulent stage into a (stable) single site structure. This is not surprising since, as was discussed in Chapter 2, (adjacent) IP excitations are found to be unstable for any $\epsilon \neq 0$ due to a positive real eigenvalue. The structure $++-$ also has adjacent IP excitations and is unstable, for any $\epsilon \neq 0$, due to a positive eigenvalue, with also a pair of bifurcating imaginary eigenvalues with negative Krein signature which eventually collide with the continuous spectrum and become complex (see Chap. 2 and [29–32]). The presence of the out-of-phase (OP) site complicates the dynamics pattern as seen in the lower left panel. The lower right panel shows the dynamics for the OP mode, $+-+$, which is stable for small couplings, but has two pairs of imaginary eigenvalues which (for larger coupling) become complex as a result of two Hamiltonian–Hopf bifurcations. This last configuration is clearly the most robust of the four ($\epsilon = 0.3$ for all configurations) since it is perturbed the most and yet persists for the longest time before turbulence sets in.

10.2.2 2(+1)*-Dimensional Solutions*

The panels depicted in this section exhibit the dynamics for the field intensity $\{|u_{\mathbf{n}}|^2\}$ for several two-dimensional configurations found in Chap. 3. As before, the value of the coupling is always beyond the threshold of instability and the configuration is perturbed by a random noise. All the dynamical evolutions are performed in a 21×21 grid. The dynamics in larger grid sizes (i.e., 31×31) were examined in a few of the cases and there was no qualitative difference found for the timescales considered herein. Each exhibited the same outcome in that one site remained for long times. A characteristic density isosurface $D_k = \{(\mathbf{n}, t) \mid |u_{\mathbf{n}}(t)|^2 = k\}$ is used here to represent the space–time evolution of the fields. The coupling and perturbation in each case were adjusted to exhibit complete destruction of the initial configuration to a single site in a reasonable time span. The details are supplied below each figure.

As already detailed in Chap. 3, the first five-site configuration, the symmetric vortices with $L = 1, M = 2$, and $L = M = 2$, as well as the asymmetric vortices with $L = 1, M = 2$, and $L = 3, M = 2$ have purely real eigenvalues. All other solutions break up due to oscillatory instability arising from Hamiltonian–Hopf bifurcations of the linearized problem when the pure imaginary eigenvalues collide with the phonon band (or continuous spectrum). The dynamical evolutions depicted in the following images qualitatively corroborate this earlier analysis. Figure 10.2 depicts the dynamical instability for the three-site configuration of Chap. 3. Next, we depict an example of the five-site configuration (lower left panel, Fig. 10.3) which exhibits complete breakdown from the initial state earlier than the other modes even

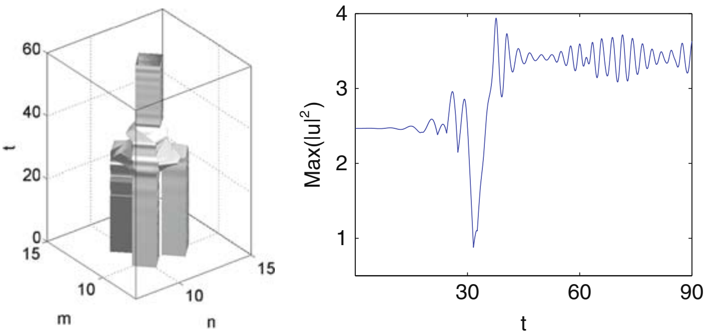

Fig. 10.2 The *left panel* shows the dynamics in time of $\{|u_{\mathbf{n}}|^2\}$ for the three-site configuration from Chap. 3 (see Eq. (3.88)). Here $\epsilon = 0.4$, the maximum of the perturbation is of amplitude $a = 10^{-4}$, and the isosurface is taken at $k = 0.2$. The *right panel*, which exhibits the maximum of the amplitude of the field intensity for this configuration up to time $t = 90$, clearly shows that the resulting single site has an oscillating amplitude ("breathes"). This can also be seen as the undulations in the isosurface picture on the *left*. Similar diagnostics confirmed this for the other cases

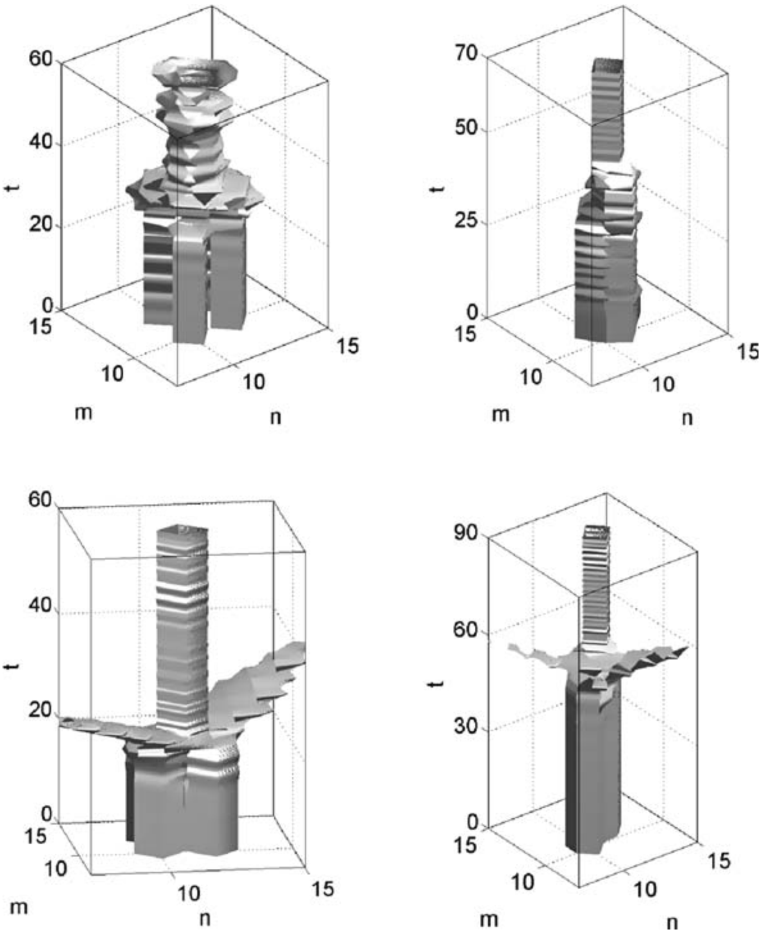

Fig. 10.3 The *two top panels* show the dynamics for the first (*top left panel*) and second (*top right panel*) four-site configurations of Eq. (3.89) in Chap. 3. The *bottom two panels* are the dynamics for the first (*bottom left panel*) and second (*bottom right panel*) five-site configurations, respectively, of the form of Eq. (3.90), Chap. 3. In each case $\epsilon = 0.4$ and the perturbation is of amplitude $a = 10^{-4}$. The isosurface is taken as $k = 0.2$ for all figures except the one at the *bottom right*, for which $k = 0.4$

though the coupling is the same and they have all been perturbed by noise with the same amplitude. This illustrates the stronger instability from purely real eigenvalues. We see a similar situation in Fig. 10.4 where the oscillatory instabilities manifest themselves in the dynamics at later times. Of the configurations in Fig. 10.4, the longest surviving one is the one with purely oscillatory instability (the symmetric vortex with $L = M = 1$ (ii)). Note that this solution is perturbed by a random noise with $a = 10^{-4}$ while the amplitude of the perturbation in (iii) is $a = 10^{-6}$. Still the solution (ii) has greater longevity.

An interesting observation is that the number of sites that remain can depend on the coupling strength and also on the magnitude of the perturbation. Take for

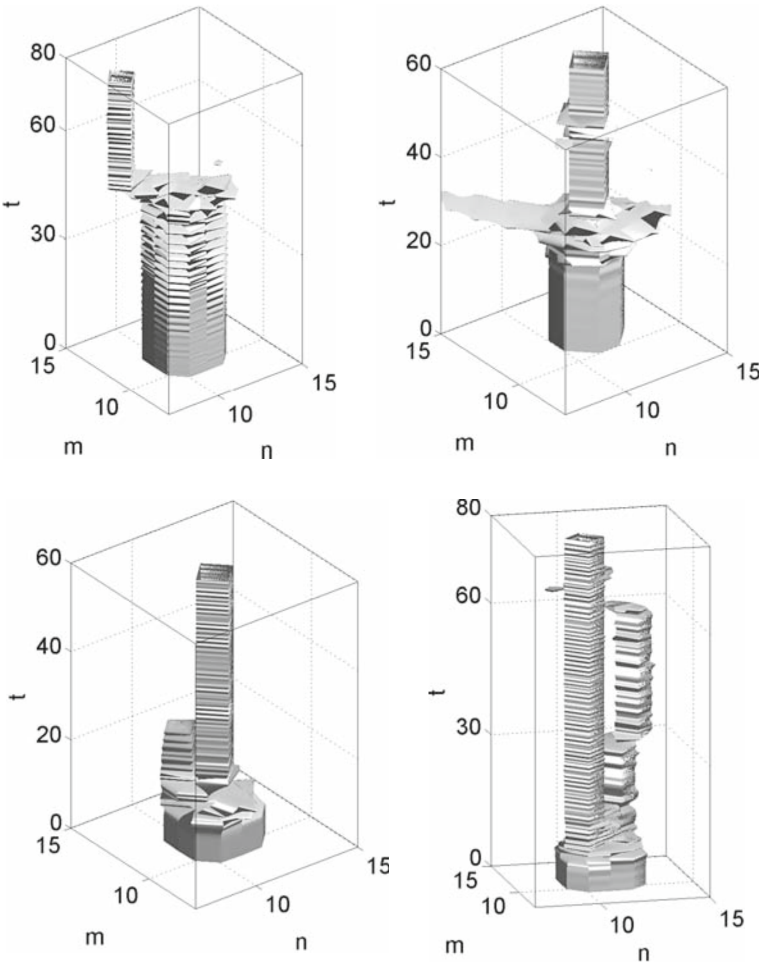

Fig. 10.4 These panels show the dynamics for the (i) nine-site configuration (*top left panel* with $a = 10^{-2}$, $k = 1.2$), and the three symmetric vortices with (ii) $L = M = 1$ (*top right panel* with $a = 10^{-4}$, $k = 0.2$), (iii) $L = 1$ and $M = 2$ (*bottom left panel* with $a = 10^{-6}$, $k = 0.7$), and (iv) $L = M = 2$ (*bottom right panel* with $a = 10^{-2}$, $k = 0.7$). In each case, $\epsilon = 0.6$

example the second five-site configuration shown in the bottom right panel of Fig. 10.3. In the figure shown, $\epsilon = 0.4$, $a = 10^{-4}$, and $k = 0.4$, and a single site remains, while for a weaker perturbation ($a = 10^{-5}$) two sites actually remain for long times. However, for a larger coupling value of $\epsilon = 0.5$ one site remains for perturbations with amplitude as small as $a = 10^{-8}$. Finally, in Fig. 10.5, we depict the dynamical instabilities for the different vortex configurations discussed in Chap. 3. Further study is needed to build on existing knowledge of discrete breathers [32, 33], in order to explain this curious interplay between the various components, and also to elucidate the underlying mechanisms responsible for these (as well as other) observations.

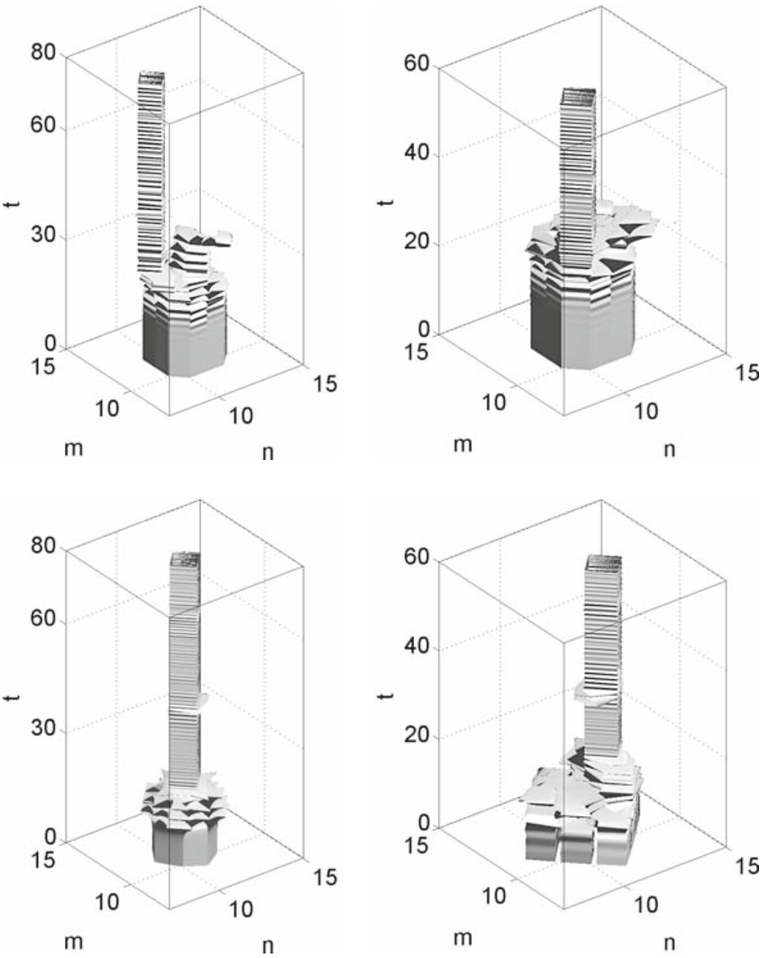

Fig. 10.5 These panels show the dynamics for the (i) symmetric vortex $L = 3$, $M = 2$ (*top left panel* with $\epsilon = 0.6$, $a = 10^{-4}$, $k = 1.2$), (ii) asymmetric vortex with $L = 1$ $M = 2$ (*top right panel* with $\epsilon = 0.6$, $a = 10^{-4}$, $k = 0.9$), (iii) asymmetric vortex with $L = 3$, $M = 2$ (*bottom left panel* with $\epsilon = 0.5$, $a = 10^{-4}$, $k = 0.7$), and (iv) vortex cross of $L = 2$ (*bottom right panel* with $\epsilon = 0.6$, $a = 10^{-2}$, $k = 0.7$). As before, these are from configurations laid out in Chap. 3

10.2.3 3(+1)*-Dimensional Solutions*

This section shows the dynamics of the field intensity, $\{|u_{\mathbf{n}}|^2\}$, for the three-dimensional configurations, the (a) diamond ($S_{\pm 1} = \{\pi/2, 3\pi/2\}$) [see Fig. 10.6], (b) octupole ($\theta_0 = \pi$, $s_0 = 1$, i.e., $S_1 = \{\pi,\ 3\pi/2,\ 0,\ \pi/2\}$) [see Fig. 10.7], and (c) double-cross ($\theta_0 = \pi$, $s_0 = 1$, i.e., $S_1 = \{\pi,\ 3\pi/2,\ 0,\ \pi/2\}$) [see Fig. 10.8]. All three of these structures were shown previously (Chap. 4) to persist. For each, we

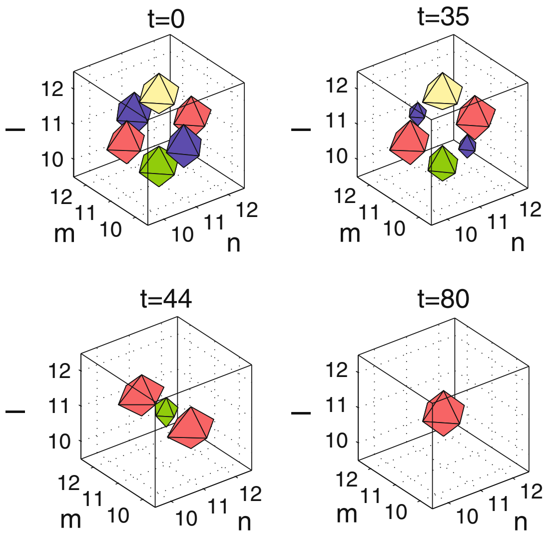

Fig. 10.6 These panels show four times in the evolution of the three-dimensional diamond structure. The coupling is taken to be $\epsilon = 0.3$, the perturbation amplitude is $a = 10^{-2}$ and and all iso-contours are taken at $\mathrm{Re}(u_{\mathbf{n}}) = \pm 0.75$ and $\mathrm{Im}(u_{\mathbf{n}}) = \pm 0.75$. The *dark gray* and *gray* are real iso-contours, while the *light* and *very light gray* are the imaginary contours

show the evolution of the instability with characteristic density isosurfaces of the three-dimensional field at four times beginning with $t = 0$.

As before, in each case a perturbation is applied at a value of the coupling well past the threshold of instability. As with the lower dimensional configurations, the coupling parameter and perturbation play a role in the evolution of the instability. For appropriate values of each, a single site will remain at the end of the time frame considered here. In the case of the octupole, it is seen that when we take $\epsilon = 0.3$

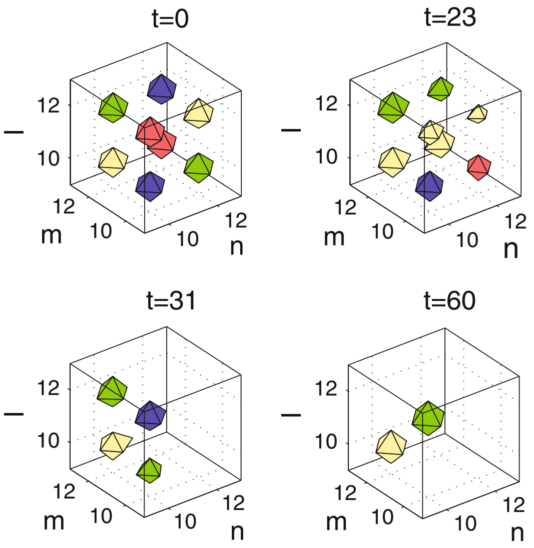

Fig. 10.7 These panels show four times in the evolution of the octupole. The coupling is $\epsilon = 0.3$, the perturbation amplitude is $a = 10^{-2}$ and and all iso-contours are taken at $\mathrm{Re}(u_{\mathbf{n}}) = \pm 0.75$ and $\mathrm{Im}(u_{\mathbf{n}}) = \pm 0.75$. The *dark gray* and *gray* are real iso-contours, while the *light* and *very light gray* are the imaginary contours

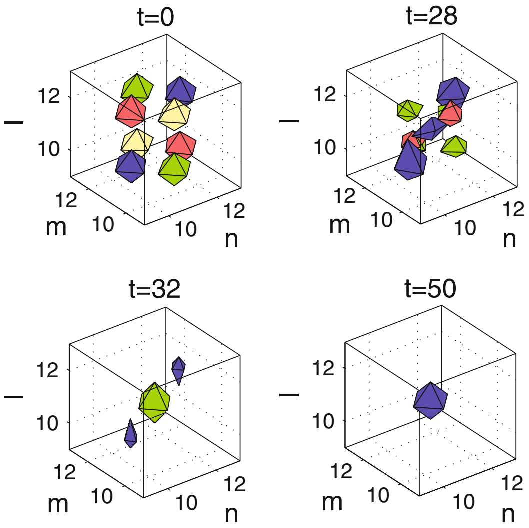

Fig. 10.8 These panels show four times in the evolution of the double cross. The coupling is $\epsilon = 0.4$, the perturbation amplitude is $a = 10^{-4}$ and and all iso-contours are taken at $\mathrm{Re}(u_{\mathbf{n}}) = \pm 0.75$ and $\mathrm{Im}(u_{\mathbf{n}}) = \pm 0.75$. The *dark gray* and *gray* are real iso-contours, while the *light* and *very light gray* are the imaginary contours

with a perturbation of amplitude $a = 10^{-2}$, two sites remain as seen in Fig. 10.7, while for $\epsilon = 0.6$ with a perturbation of amplitude $a = 10^{-4}$, a single site remains. A similar phenomenon is observed for the double cross where for $\epsilon = 0.3$ with a perturbation of amplitude $a = 10^{-2}$, two sites remain as seen in Fig. 10.8, while for $\epsilon = 0.4$ with a perturbation of amplitude $a = 10^{-4}$, a single site remains.

In all cases, the grid size is $21 \times 21 \times 21$. It should be noted that for the diamond configuration, larger grid sizes (i.e., $25 \times 25 \times 25$, $27 \times 27 \times 27$) were examined, with no qualitative change in behavior witnessed. In each case, the end result for a given coupling and perturbation was always the same number of surviving sites.

10.3 Non-Standard Scenario

We will now consider a few more exotic settings. First, we look at the vortex solutions with a six neighbor hexagonal geometry as seen in the end of Chap. 3. Then, we will look at the same DNLS equation (10.1), except with a defocusing nonlinearity ($g = 1$) in 1(+1) and 2(+1) dimensions from Chap. 5.

10.3.1 Hexagonal Lattice

In this section we consider the variation of Eq. (10.1) in which the terms $\Delta_d u_{\mathbf{n}}$ are replaced by the non-standard extrapolation of the two-dimensional five-point stencil, in which each site has four neighbors as in the previous section and following subsection, to the natural variation for the six-neighbor lattice, $\sum_{\langle \mathbf{n}' \rangle} u_{\mathbf{n}'} - 6u_{\mathbf{n}}$, where $\langle \mathbf{n}' \rangle$ is the set of nearest neighbors to the node indexed by $\mathbf{n}$.

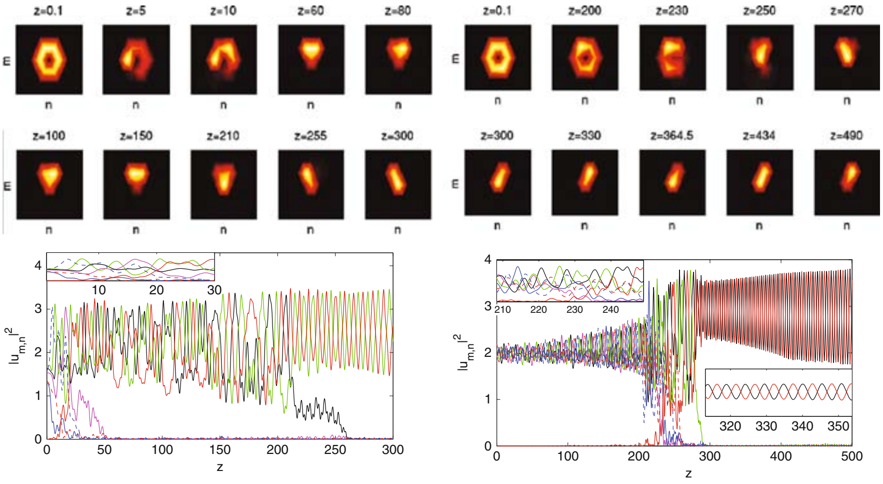

Fig. 10.9 Space–time evolution of $\{|u_{\mathbf{n}}(t)|^2\}$, where the lattice geometry is hexagonal, $\mathbf{u} = \mathbf{u}_s(1 + \max_{\mathbf{n}}\{|u_{\mathbf{n},s}(0)|^2\}\mathbf{u}_r)$, $\mathbf{u}_r$ is a uniform random variable in $(-0.05, 0.05)$ random variable, and $\mathbf{u}_s$ is a single charged vortex on the *left* ($\epsilon = 0.1$) and a double charged vortex on the *right* ($\epsilon = 0.125$). The *top panels* are snapshots and the *bottom* are amplitudes of the individual excited sites. Note the almost harmonic oscillations depicted in the inset of the *bottom right*

The vortex solutions in this geometry are displayed at the end of Chap. 3. The single charged vortex is actually more unstable than the double charged one (the eigenvalues bifurcating from the origin in the AC limit are real for the former and imaginary for the latter). The dynamics of these solutions given in Fig. 10.9 confirm this theoretical prediction. The single charged vortex ($\epsilon = 0.1$) breaks up very rapidly before $z = 20$ and subsequently degenerates into a lopsided dipole-type configuration, while the double charged vortex ($\epsilon = 0.125$) persists until well past $z = 200$. Each configuration ultimately becomes a two-site breather for long distances, with one site being the initially unpopulated center site.

10.3.2 Defocusing Nonlinearity

We now study the dynamics of typical 1(+1)- and 2(+1)-dimensional solutions with defocusing nonlinearity ($g = +1$ in Eq. (10.1)).

10.3.2.1 1(+1)-Dimensional Solutions

We begin by examining the dynamics of the unstable one-dimensional configurations. Two one-dimensional dark soliton configurations with defocusing nonlinearity are principally considered in this book; in both cases the absolute value squared of the background is one and there is a π phase jump, which can either occur between two sites (IS) or between three sites (on-site, OS), where there exists a node with zero amplitude in the middle of the latter. As shown in Chap. 5, the OS dark soliton is stable for small coupling, and subject only to oscillatory instability (as the coupling increases) due to complex quartets of eigenvalues which emerge when the null eigenvalues from the AC limit with negative Krein signature reaches the continuous spectrum, at which point Hamiltonian–Hopf bifurcations occur . On the other hand, the pair which bifurcates from the spectral plane origin (at the AC limit) in the case of the IS configuration becomes real and therefore this configuration is subject to a strong (exponential) instability.

Figure 10.10 shows the space–time evolution of the dark solitons which confirm the theoretical and numerical predictions. The left panel shows the solution $\mathbf{u} = \mathbf{u}_s + \mathbf{u}_r$ where $\mathbf{u}_s$ is the IS dark soliton and $\mathbf{u}_r$ is random noise field uniformly distributed in the interval $(-5, 5) \times 10^{-4}$. Note even with such a mild perturbation from the stationary state, this configuration disintegrates after $t = 20$. On the other hand, in the right panel $\mathbf{u}_s$ is the OS configuration with $\mathbf{u}_r$ uniformly distributed in the interval $(-5, 5) \times 10^{-2}$, and yet the original configuration persists until $t = 500$. This not only confirms, but really highlights the accuracy of the theoretical stability calculations from Chap. 5, Sect. 5.1.2.

10.3.2.2 2(+1)-Dimensional Solutions

Next, we will consider the two-dimensional configurations from Chap. 5, Sect. 5.2. As in the one-dimensional case described above, the configurations $\mathbf{u}_s$ are perturbed by a field $\mathbf{u}_r$ randomly distributed in the interval $(-5, 5) \times 10^{-2}$. The same field $\mathbf{u}_r$ is added to each solution for consistency so they may be more easily compared (and it is so large because the least stable among these configurations took a considerable time to degenerate even with this perturbation). We present the results of the dynamical evolution of the two-site, four-site, and $S = 1$ vortices organized with

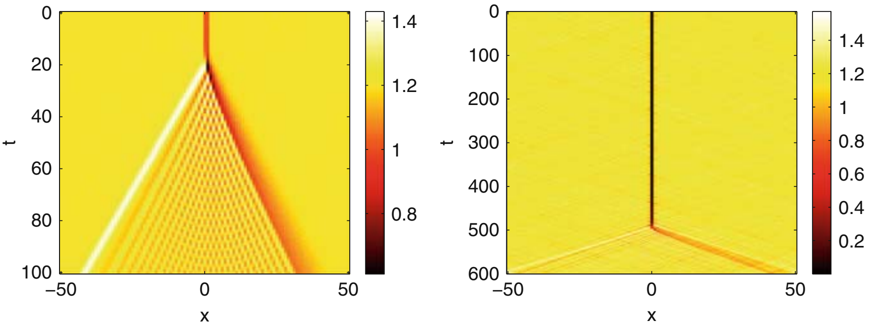

Fig. 10.10 Dynamics of the inter-site (*left*) and on-site (*right*) dark soliton configurations are represented by space–time plots of the intensity of the field $\{|u_{\mathbf{n}}(t)|^2\}$ as defined in the previous section with $\epsilon = 0.1$. These solutions correspond to those in Chap. 5, where the inter-site one is perturbed by a random noise of only $\pm 5 \times 10^{-4}$, and is visibly distorted by $t = 20$, while the on-site configuration is perturbed by a noise amplitude of $\pm 5 \times 10^{-2}$ and yet the original configuration persists until $t = 500$

the IS solutions in the left column, the OS solutions in the right column, and, for the former two, the top are IP, and the bottom are OP. Again as in Sect. 10.2.2, we choose density isosurfaces, $D_k = \{(\mathbf{n}, t) \mid |u_{\mathbf{n}}(t)|^2 = k\}$ as our visualization tool. The magnitude of the density isosurface k is chosen as half the maximum of the initial density field $k = (1/2)|u_{\mathbf{n}}(0)|^2$ in most cases, except when a smaller magnitude was necessary to visualize the relevant dynamics. All solutions degenerate into a single site configuration for long times, although it is worth mentioning here that, as in the focusing case, for smaller coupling values than those chosen here (but still significantly far from the AC limit), even unstable solutions may only undulate and not actually break up at all.

The two-site configurations are given in Fig. 10.11. Results confirm the stability analysis in Chap. 5, Sect. 5.3.2. In particular, note that the mild instability of the ISIP

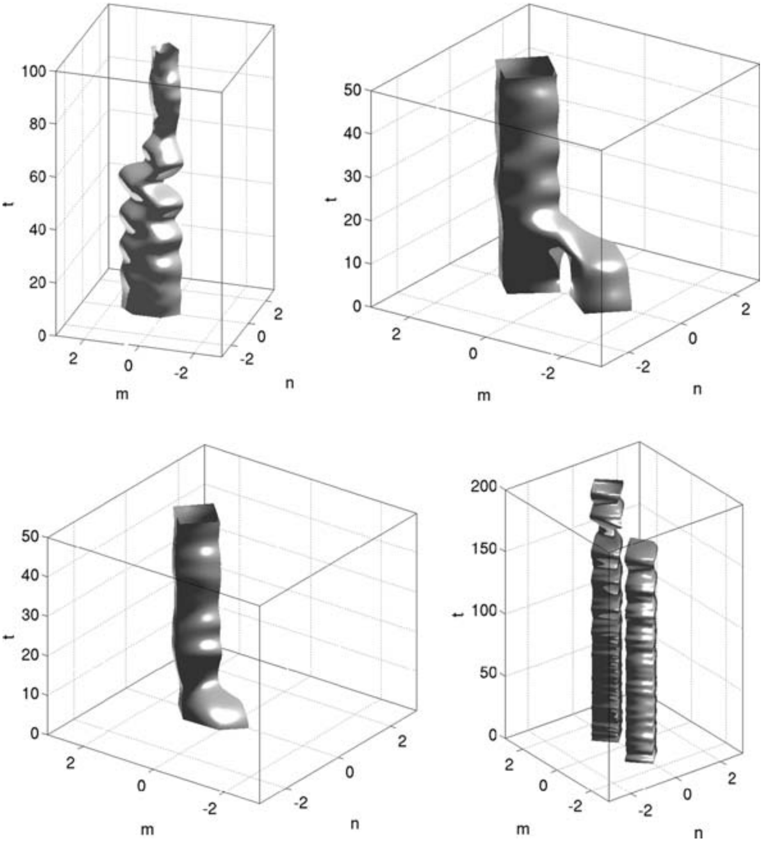

Fig. 10.11 Given above are the space–time evolutions of $\{|u_{\mathbf{n}}|^2\}$ as given before where $\mathbf{u}_s$ are the two-dimensional dipole configurations for defocusing nonlinearity. The *top row* is in-phase, the *bottom row* is out-of-phase, the *left column* is inter-site, and the *right column* is on-site. These solutions correspond to those found in Chap. 5, Sect. 5.2, for the coupling values (clockwise from *top left*) $\epsilon = 0.116, 0.08, 0.116$, and 0.08

solution for $\epsilon = 0.116$ given in the upper left panel takes a considerable amount of time to break up the initial configuration as compared to the strong instability of the ISOP for $\epsilon = 0.08$ in the bottom left, which leads to degeneration almost immediately into a single site upon evolution. In the right column we can see the fast degeneration of the OSIP for $\epsilon = 0.08$ as a manifestation of the strong instability on the top row and the much slower degeneration of the OSOP for $\epsilon = 0.116$ depicting the oscillatory Hamiltonian–Hopf instability on the bottom.

Figure 10.12 depicts the quadrupole solutions, which again confirm the theoretical and numerical findings of Chap. 5, Sect. 5.3.3. The more stable ISIP ($\epsilon = 0.1$)

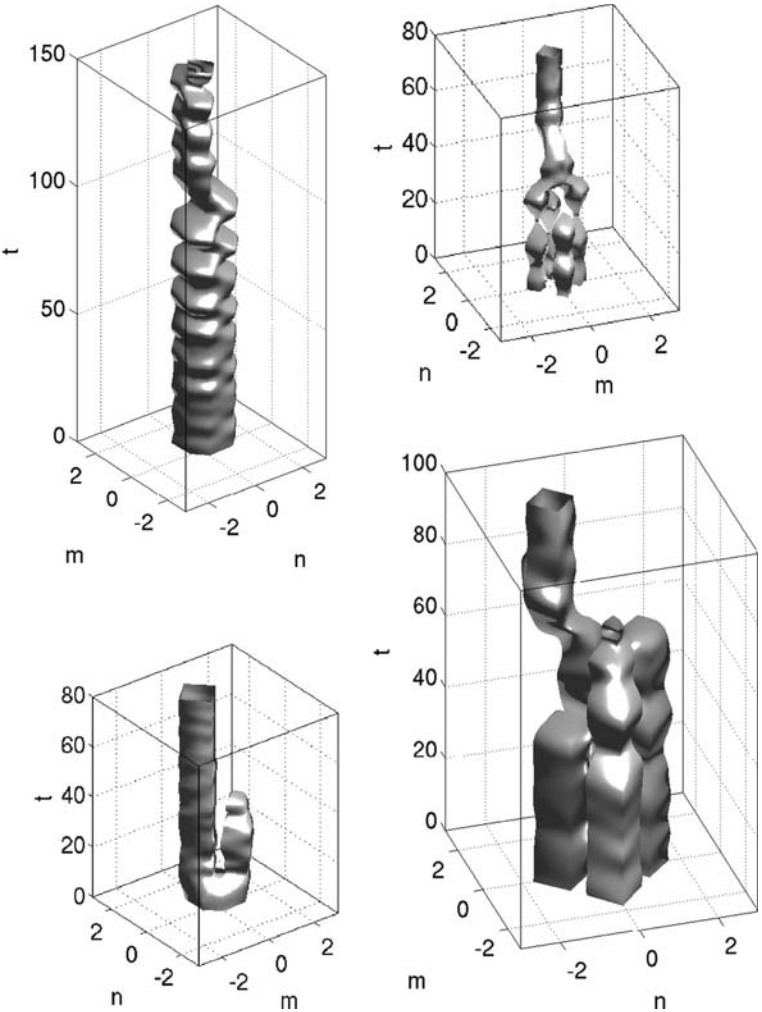

Fig. 10.12 Same as Fig. 10.11, except for the relevant four-site configurations given in Chap. 5, Sect. 5.3 and the coupling value is $\epsilon = 0.1$ for all panels

in the upper left panel and OSOP ($\epsilon = 0.1$) in the lower right panel confirm the predictions. So do the more unstable OSIP and ISOP (both for $\epsilon = 0.1$) in the top right and bottom left panels, respectively. For this coupling value, the ultimate single site configuration of the ISOP is robust to perturbation (down to 10^{-8}), as was the second five-site configuration presented in Sect. 10.2.2. Again for a slightly smaller coupling of $\epsilon = 0.08$, a two-site configuration remains, which breathes up to at least $t = 900$ (not shown), and again there is a larger perturbation which spoils the breathing two-site structure for this coupling. Additionally, on investigating the intermediate coupling value of $\epsilon = 0.9$, one finds that the perturbation necessary to break the two-site structure becomes smaller, suggesting that the necessary perturbation to eliminate the breather is inversely proportional to the coupling prior to the lower bound of the region in coupling space for which a single site invariably survives. Also, for $\epsilon = 0.05$ the OSIP remains a breathing four-site structure even for longer times despite the strong instability of the linearization and almost instantaneous breathing behavior. This again supports the same hypothesis mentioned above. Finally, Fig. 10.13 shows the single charge vortex solutions from Chap. 5, Sect. 5.3.4. Both of these solutions are approximately equivalently unstable. Each has both Hamiltonian–Hopf quartets and real pairs of eigenvalues.

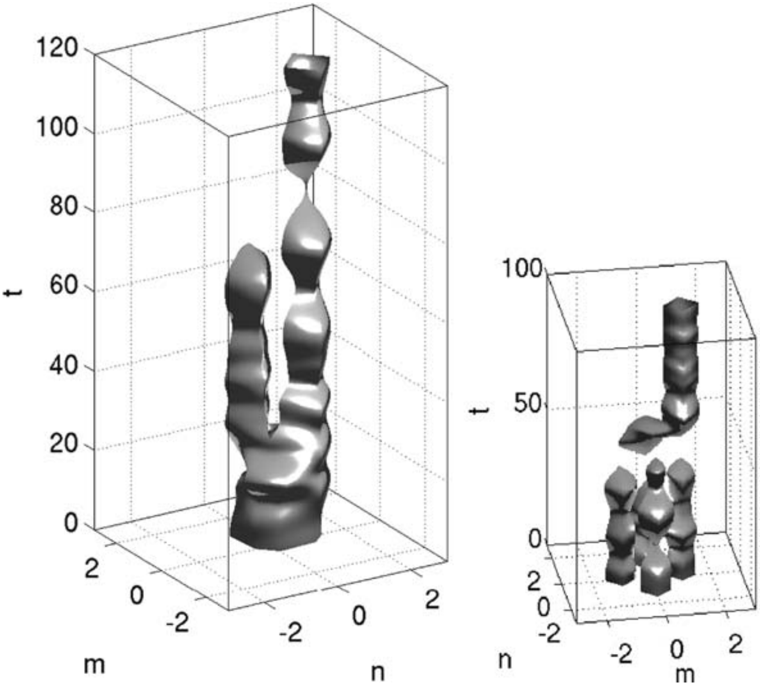

Fig. 10.13 Dynamics of the two-dimensional charge 1, four-site gap vortices with defocusing nonlinearity. The inter-site version is on the *left*, while the on-site version is on the *right* and $\epsilon = 0.1$ in both cases

10.4 Conclusion and Future Challenges

We have numerically examined the dynamics of discrete solitons for the DNLS equation in one, two, and three spatial dimensions with the standard focusing nonlinearity. We also investigated the more exotic hexagonal lattice and the case of defocusing nonlinearity, the latter of which has been observed in the experimental setting of nonlinear optics [34, 35]. It is found that the numerical dynamics aligns itself with the theoretical predictions for linear stability established in the previous chapters. It is noted that the dynamics within the timescales considered here depend not only on the linear stability, but also sensitively on the coupling parameter and (to a lesser degree) on the perturbation. For each case, there exists some coupling and perturbation such that the eventual result is a single robust site (as displayed in the images).

A major challenge for the future would be to devise and further develop a theoretical framework to understand [33] the instability process. The single site is an attractive equilibrium of the system. Since it is stable and has low energy, it is no surprise that an unstable system would tend to this state. But, it would be interesting to attempt to develop some more precise theory relating these aspects of the nonlinear evolution and perhaps elucidate general characteristics and features that may not be visible from the numerics. It would also be of interest to examine more complex systems, such as multicomponent and higher dimensional systems, and to determine whether some general features persist.

Acknowledgments K.J.H.L. would like to extend his grateful appreciation to P.G. Kevrekidis, first and foremost, not only for the endless stream of advising during the revision process of the current work, but also for the financial support that enabled its completion. He would also like to acknowledge UMass for the office and mathematical support. Q.E.H. is grateful for the opportunity to work on this project.

References

1. Dodd, R.K., Eilbeck, J.C., Gibbon, J.D., Morris, H.C.: Solitons and Nonlinear Wave Equations. Academic Press, London (1982) 205
2. Krumhansl, J.A.: The intersection of nonlinear science, molecular biology, and condensed matter physics. Viewpoints. In: Nonlinear Excitations in Biomolecules. Peyrard, M. (ed.), Springer-Verlag, Berlin and les Editions de Physique, Les Ulis, 1–9, (1995). 205
3. Remoissenet, M.: Waves Called Solitons: Concepts and Experiments. Springer, NewYork (1999) 205
4. Kevrekidis, P.G., Rasmussen, K.Ø., Bishop, A.R.: Int. J. Mod. Phys. B **15**, 2833–2900 (2001) 205
5. Scott, A.: Nonlinear Science: Emergence and Dynamics of Coherent Structures. Oxford Texts in Applied and Engineering Mathematics, London (2003) 205
6. Dauxois, T., Peyrard, M.: Physics of Solitons. Cambridge University Press, NewYork (2006) 205
7. Careri, G., Buontempo, U., Galluzzi, F., Scott, A.C., Gratton, E., Shyamsunder, E.: Phys. Rev. B **30**, 4689–4702 (1984) 205
8. Feddersen, H.: Phys. Lett. A **154**, 391–395 (1991) 205
9. Eisenberg, H.S., Silberberg, Y., Morandotti, R., Boyd, A.R., Aitchison, J.S.: Phys. Rev. Lett. **81**, 3383–3386 (1998) 205

10. Binder, P., Abraimov, D., Ustinov, A.V.: Phys. Rev. E **62**, 2858–2862 (2000) 205
11. Trombettoni, A., Smerzi, A.: Phys. Rev. Lett. **86**, 2353–2356 (2001) 205
12. Christodoulides, D.N., Joseph, R.I.: Opt. Lett. **13**, 794–796 (1988) 205
13. Davydov, A.S.: J. Theor. Biol. **38**, 559–569 (1973) 205
14. Frenkel, J., Kontorova, T.: J. Phys. (USSR) **1**, 137–149 (1939) 205
15. Fermi, E., Pasta, J.R., Ulam, S.M.: Studies of Nonlinear Problems. Los Alamos Sci. Lab. Rep. LA-1940, (1955), published later in Collected Papers of Enrico Fermi, Serge, E. (ed.), University of Chicago Press, NewYork (1965) 205
16. Toda, M.: Theory of Nonlinear Lattices. Springer-Verlag, Berlin (1981) 205
17. Carr, J., Eilbeck, J.C., Phys. Lett. A **109**, 201–204 (1985) 205
18. Mackay, R.S., Aubry, S.: Nonlinearity **7**, 1623–1643 (1994) 205
19. Efremidis, N.K., Sears, S., Christodoulides, D.N., Fleischer, J.W., Segev, M.: Phys. Rev. E **66**, 046602 (2002) 205
20. Kivshar, Y.S., Agrawal, G.P., Optical Solitons: From Fibers to Photonic Crystals. Academic Press, NewYork (2003) 205
21. Ablowitz, M.J., Prinari, B., Trubatch, A.D.: Discrete and Continuous Nonlinear Schrödinger Systems. London Mathematical Society Lecture Note Series 302, Cambridge University Press, NewYork (2004) 205
22. Makris, K.G., Suntsov, S., Christodoulides, D.N., Stegeman, G.I., Heche, A., Opt. Lett. **30**, 2466 (2005) 205
23. Bludov, Yu.V., Konotop, V.V.: Phys. Rev. E **76**, 046604 (2007) 205
24. Susanto, H., Kevrekidis, P.G., Carretero-González, R., Malomed, B.A., Frantzeskakis, D.J.: Phys. Rev. Lett. **99**, 214103 (2007) 205
25. Kevrekidis, P.G., Frantzeskakis, D.J., Carretero-González, R.: Emergent Nonlinear Phenomena in Bose-Einstein Condensates: Theory and Experiment. Springer Series on Atomic, Optical, and Plasma Physics, vol. 45, (2008) 205
26. Hoq, Q.E., Gagnon, J., Kevrekidis, P.G., Malomed, B.A., Frantzeskakis, D.J., Carretero-González, R.: Extended Nonlinear Waves in Multidimensional Dynamical Lattices. Math. Comput. Simulat. 2009 205
27. Hoq, Q.E., Gagnon, J., Kevrekidis, P.G., Malomed, B.A., Frantzeskakis, D.J., Carretero-González, R.: http://www-rohan.sdsu.edu/∼rcarrete/ 205
28. Hoq, Q.E., Carretero-González, R., Kevrekidis, P.G., Malomed, B.A., Frantzeskakis, D.J., Bludov, Yu.V., Konotop, V.V.: Phys. Rev. E **78**, 036605 (2008) 205
29. Pelinovsky, D.E., Kevrekidis, P.G., Frantzeskakis, D.J.: Physica D **212**, 1–19 (2005) 206, 207
30. Pelinovsky, D.E., Kevrekidis, P.G., Frantzeskakis, D.J.: Physica D **212**, 20–53 (2005) 206, 207
31. Kapitula, T., Kevrekidis, P.G., Sandstede, B.: Physica D **195**, 263–282 (2004) 207
32. Aubry, S.: Physica D **103**, 201–250 (1997) 207, 210
33. Alfimov, G.L., Brazhnyi, V.A., Konotop, V.V.: Physica D **194**, 127–150 (2004) 210, 219
34. Tang, L., Lou, C., Wang, X., Chen, Z., Susanto, H., Law, K.J.H., Kevrekidis, P.G.: Opt. Lett. **32**, 3011–3013 (2007) 219
35. Song, D., Tang, L., Lou, C., Wang, X., Xu, J., Chen, Z., Susanto, H., Law, K.J.H., Kevrekidis, P.G.: Opt. Exp. **16**, 10110–10116 (2008) 219